ACS APPLIED MATERIALS & INTERFACES

www.acsami.org

Forum Article

# Enhanced Photocatalytic Alcohol Oxidation at the Interface of RuC-Coated $TiO_2$ Nanorod Arrays

Shuya Li, Eric Wolfgang Shuler, Debora Willinger, Hai Tien Nguyen, Saerona Kim, Hyeong Cheol Kang, Jae-Joon Lee, Weiwei Zheng, Chang Geun Yoo, Benjamin D. Sherman, and Gyu Leem*

Cite This: *ACS Appl. Mater. Interfaces* 2022, 14, 22799–22809

Read Online

ACCESS | Metrics & More | Article Recommendations | Supporting Information

**ABSTRACT:** Visible-light-driven organic oxidations carried out under mild conditions offer a sustainable approach to performing chemical transformations important to the chemical industry. This work reports an efficient photocatalytic benzyl alcohol oxidation process using one-dimensional (1D) $TiO_2$ nanorod (NR)-based photoanodes with surface-adsorbed ruthenium polypyridyl photocatalysts at room temperature. The photocatalyst bis(2,2′-bipyridine)(4,4′-dicarboxy-2,2′-bipyridine)Ru(II) (RuC) was covalently anchored onto $TiO_2$ nanorod arrays grown on fluorine-doped tin oxide (FTO) electrode surfaces (FTO|t-$TiO_2$|RuC, $t$ = the thickness of $TiO_2$ NR). Under aerobic conditions, the photophysical and photocatalytic properties of FTO|t-$TiO_2$|RuC ($t$ = 1, 2, or 3.5 $\mu$m) photoanodes were investigated in a solution containing a hydrogen atom transfer mediator (4-acetamido-2,2,6,6-tetramethylpiperidine-N-oxyl, ACT) as cocatalyst. Dye-sensitized photoelectrochemical cells (DSPECs) using the FTO|t-$TiO_2$|RuC ($t$ = 1, 2, or 3.5 $\mu$m) photoanodes and ACT-containing electrolyte were investigated for carrying out photocatalytic oxidation of a lignin model compound containing a benzylic alcohol functional group. The best-performing anode surface, FTO|1-$TiO_2$|RuC (shortest NR length), oxidized the 2° alcohol of the lignin model compound to the $C_\alpha$-ketone form with $a$ > 99% yield over a 4 h photocatalytic experiment with a Faradaic efficiency of 88%. The length of $TiO_2$ NR arrays ($TiO_2$ NRAs) on the FTO substrate influenced the photocatalytic performance with longer NRAs underperforming compared to the shorter arrays. The influence of the NR length is hypothesized to affect the homogeneity of the RuC coating and accessibility of the ACT mediator to the RuC-coated $TiO_2$ surface. The efficient photocatalytic alcohol oxidation with visible light at room temperature as demonstrated in this study is important to the development of sustainable approaches for lignin depolymerization and biomass conversion.

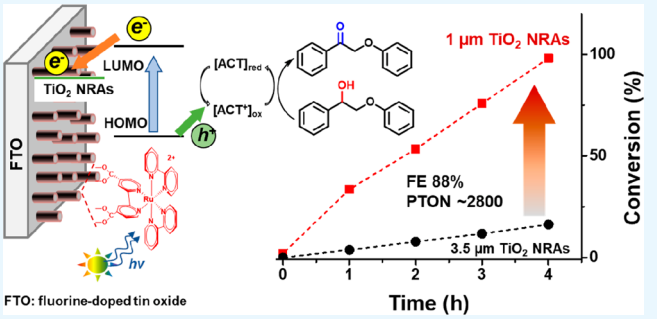


**KEYWORDS:** *dye-sensitized photoelectrosynthesis cell, $TiO_2$ nanorods, lignin conversion, mild conditions, photo-oxidation, alcohol dehydrogenation*



## INTRODUCTION

Dye-sensitized photoelectrochemical cells (DSPECs) based on wide bandgap n- and p-type semiconductors have been intensively studied for solar-light-induced water splitting reactions coupled to (photo)catalysts.[1−8] In the case of DSPECs for water splitting, water is oxidized to $O_2$ at the photoanode and the proton equivalents are reduced at the (photo)cathode.[9] By replacing water oxidation, selective organic molecules (e.g., benzyl alcohols) were similarly oxidized at the photoanode in an aqueous DSPEC upon light illumination.[10,11] This light-driven approach to alcohol oxidation offers an attractive and cost-effective route for controlled alcohol dehydrogenation and presents an alternate application for DSPECs outside of water splitting for the production of solar fuels.

Lignocellulosic biomass including cellulose, hemicellulose, and lignin represents a potential substitute for petroleum-based carbon sources by converting to value-added fuels and commodity chemicals.[12,13] Lignin valorization through conversion to low-molecular-weight aromatic compounds has been considered as a sustainable alternative source to petroleum for the chemical industry.[14,15] Recent studies for lignin valorization have focused on chemical, electrochemical, and/or photocatalytic strategies for depolymerization under mild conditions to produce well-defined and targeted value-added aromatic chemical building blocks.[16−20] In particular, oxidation of the 2° benzylic $C_\alpha$−OH alcohol in the $\beta$-aryl ether linkage, which is the most abundant linkage in lignin, is a critical step toward cleaving the lignin polymer backbone to produce

**Special Issue:** Early Career Forum

**Received:** October 27, 2021
**Accepted:** February 14, 2022
**Published:** February 23, 2022

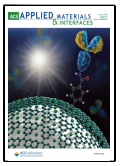




https://doi.org/10.1021/acsami.1c20795
*ACS Appl. Mater. Interfaces* 2022, 14, 22799−22809

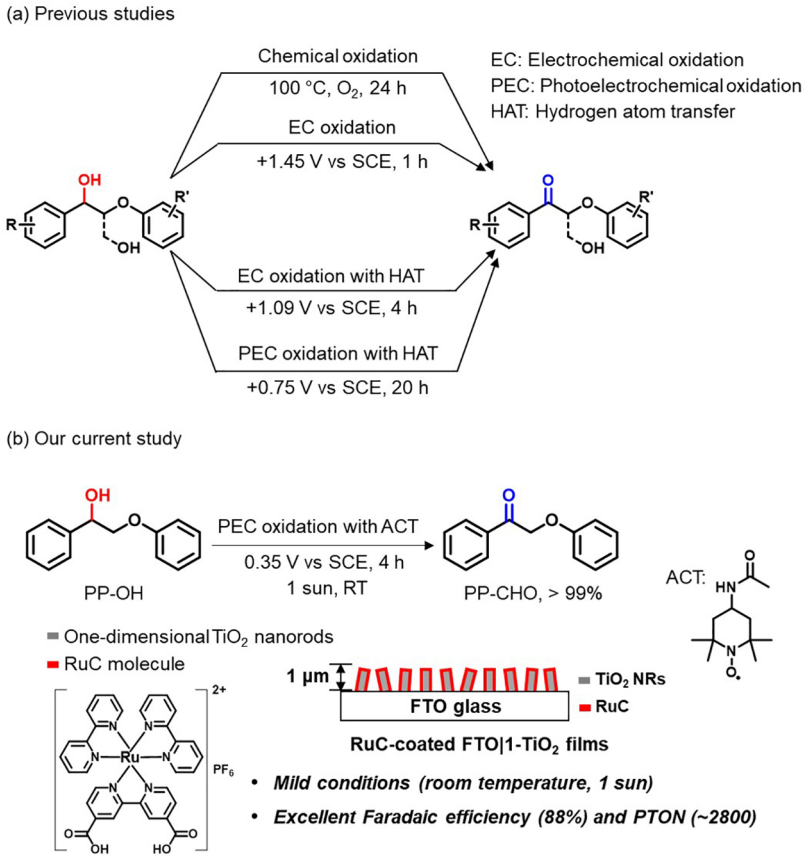


**Figure 1.** (a) Reported benzylic alcohol oxidation strategies of lignin model compounds with chemical, electrochemical (EC), photoelectrochemical (PEC), and HAT-assisted PEC pathways.[14,15,21,23] (b) Our current study for benzylic alcohol oxidation of a lignin model compound, PP-OH, using a RuC-coated 1D $TiO_2$ NRA (with the vertical height 1, 2, or 3.5 $\mu$m) on fluorine-doped tin oxide (FTO) coupled with an ACT mediator under the applied bias of 0.35 V vs SCE.

targeted aromatic compounds. Previous studies have reported the chemical, electrochemical, or photoelectrochemical oxidation of the benzylic $C_\alpha$−OH group in lignin model compounds with the use of nitroxyl radicals (e.g., 2,2,6,6-tetramethylpiperidine-N-oxyl (TEMPO), *N*-hydroxyphthalimide (NHPI)) as a hydrogen atom transfer mediator (HAT) (Figure 1).[18,21−23] The importance of the HAT mediator is demonstrated by comparing the onset of electrocatalytic alcohol oxidation of the benzylic $C_\alpha$−OH in its absence (1.45 V vs SCE) to that in the presence of a HAT mediator (1.09 V vs SCE). Furthermore, our recent study focused on photoelectrochemical oxidation of the $C_\alpha$−OH in lignin models containing a 2° benzylic alcohol in a mesoporous nanoparticle-type $TiO_2$ (meso-$TiO_2$) DSPEC with a lower bias of 0.75 V vs SCE.[14] This study used NHPI as the HAT mediator in the presence of a base and achieved 90% conversion of the $C_\alpha$−OH to the ketone form, $C_\alpha$=O, over a 20 h photochemical experiment under an applied bias of 0.75 V vs SCE in mild conditions (e.g., room temperature, air atmosphere, no sacrificial donor/acceptors) (Figure 1a).

This report presents an improved heterogeneous photocatalytic approach to oxidize the benzylic alcohols in a lignin model compound, 2-phenoxy-1-phenylethanol (PP-OH) using a 1D rutile $TiO_2$ nanorod array ($TiO_2$ NRA) based DSPEC incorporating the HAT mediator, 4-acetamido-2,2,6,6-tetramethylpiperidine-N-oxyl (ACT) (Figure 1b). It is noted that DSPEC systems using dye-coated mesoporous structured $TiO_2$ films have previously been used for phenol and benzyl alcohol oxidation in the aqueous phase.[5,24] $TiO_2$ NR surfaces have been shown to improve charge transport from the solution interface to the transparent conductive oxide surface, resulting in enhancement of the photovoltaic efficiency compared to the commonly used meso-$TiO_2$ films.[25] Visible-light-induced photocatalysis can be utilized for a variety of organic transformation.[26,27] As a photocatalyst, a carboxylic-acid-functionalized polypyridyl ruthenium(II) complex (bis(2,2′-bipyridine)(4,4′-dicarboxy-2,2′-bipyridine)Ru(II), (RuC)) was used here by adsorption to $TiO_2$ NRA-coated fluorine-doped tin oxide (FTO|$TiO_2$) electrodes. Polypyridyl Ru(II) complexes have been widely used for various applications including water splitting and lignin depolymerization because of the high absorptivity in the visible region and long-lived excited-state lifetimes.[7,28−31] The RuC-modified FTO|t-$TiO_2$ ($t$ = the thickness of $TiO_2$ NRA on FTO) surface (FTO|t-$TiO_2$|RuC) coupled with ACT in solution achieved $a$ > 99% conversion of the lignin model compound, PP-OH, to the oxidized ketone form, 2-phenoxy-1-phenoylethanone (PP-CHO), in just 4 h at an applied bias of 0.35 V vs SCE under the visible-light illumination (1 sun) at room temperature. The photoelectrochemical properties of the FTO|t-$TiO_2$|RuC surface using three different $TiO_2$ NRA heights ($t$ = 1, 2, 3.5 $\mu$m) were studied to elucidate the mechanistic pathway of benzylic alcohol oxidation in the presence of ACT.

## RESULTS AND DISCUSSION

The $TiO_2$ NRA electrodes were prepared by the direct growth of the nanorods on the FTO surface by modifying a


https://doi.org/10.1021/acsami.1c20795
ACS Appl. Mater. Interfaces 2022, 14, 22799−22809

conventional $TiO_2$ nanoparticle seed-layer precoating method.[32] The morphology and vertical height of the $TiO_2$ NRA layer were controlled by the different reaction temperatures (e.g., 135, 150, or 170 °C) used during the hydrothermal reaction.[33] The average diagonal and vertical height of the $TiO_2$ NR on FTO were characterized by scanning electron microscopy (SEM) (Figure S1). The corresponding average diagonal size (plane-view) of the $TiO_2$ NRA were approximately 67, 97, and 133 nm which corresponded to the surfaces with vertical heights (cross-section view) of 1, 2, and 3.5 $\mu$m, respectively. Figure 2 shows plane view images and nanorod

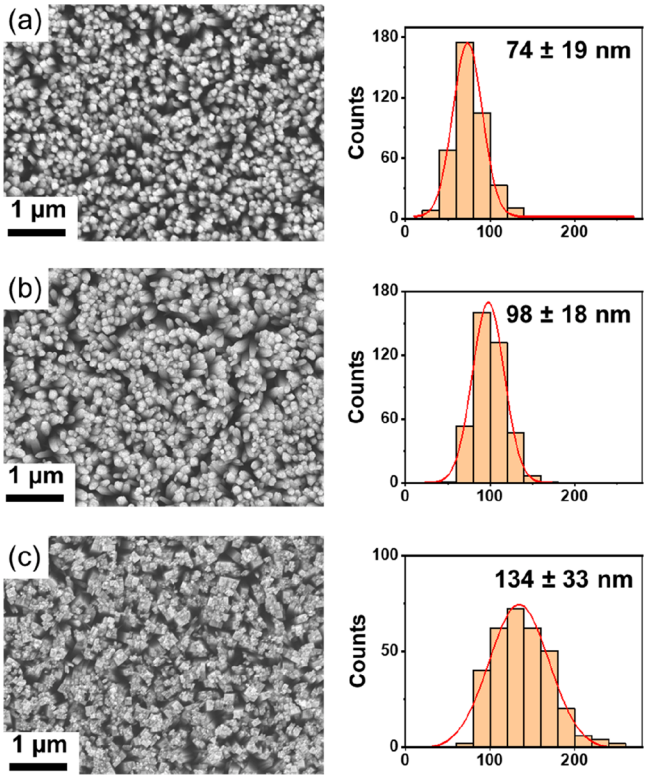


**Figure 2.** SEM images (plane-view) of RuC covalently immobilized onto (a) FTO|1-$TiO_2$, (b) FTO|2-$TiO_2$, and (c) FTO|3.5-$TiO_2$. Size distributions of nanorod diameters for each type of $TiO_2$ NRA surface are shown.

diameter distributions after the immobilization of RuC onto the FTO|t-$TiO_2$ ($t$ = 1, 2, or 3.5 $\mu$m) surface. The average diagonal sizes of the RuC-coated $TiO_2$ NRAs were approximately 74, 98, and 134 nm for FTO|1-$TiO_2$ |RuC, FTO|2-$TiO_2$|RuC, and FTO|3.5-$TiO_2$|RuC, respectively, which are roughly similar to that of undyed FTO|t-$TiO_2$ surface. Profilometry measurements of the RuC-modified surfaces corroborated the film heights determined by SEM with average heights of 0.93, 2.25, and 3.47 $\mu$m found by profilometry as shown in Table S1.

Next, the photophysical properties of the FTO|t-$TiO_2$|RuC electrodes were investigated to elucidate the process of charge transfer between the 1D t-$TiO_2$ interface and RuC. Figure 3a shows the UV−vis spectra of the FTO|t-$TiO_2$|RuC electrodes, indicating a strong d$\pi$ (Ru) → $\pi^*$ (bipyridine, bpy) metal-to-ligand charge transfer (MLCT) absorption band at $\lambda_{max} \approx$ 430−463 nm in the visible region. The MLCT of RuC powder was observed at $\lambda_{max} \approx$ 466 nm. Interestingly, as the thickness of t-$TiO_2$ increases, the MLCT absorption bands from FTO|t-$TiO_2$|RuC films exhibited blue-shifted absorption peaks with $\lambda_{max} \approx$ 463, 446, and 430 nm for FTO|1-$TiO_2$|RuC, FTO|2-$TiO_2$|RuC, and FTO|3.5-$TiO_2$|RuC, respectively. A previous study reported that a blue-shift in the UV−vis absorption peaks of dyes on a $TiO_2$ surface is caused by the formation of H-aggregates during the sensitization process.[34] Thus, the formation of aggregates and a change in the interaction of the RuC photocatalyst on the $TiO_2$ surface would occur with an increase in the vertical height and width of the $TiO_2$ nanorods on FTO substrate.[25,34,35] In Figure 3b, photoluminescence emission spectra show broad and distinguished intense peaks with $\lambda_{max} \approx$ 688, 675, 667, and 657 nm for RuC powder, FTO|1-$TiO_2$|RuC, FTO|2-$TiO_2$|RuC, and FTO|3.5-$TiO_2$|RuC, respectively, arising from the MLCT excited state. These blue shifts of the steady-state emissions of the FTO|t-$TiO_2$|RuC films as compared to RuC powder are in good agreement with the previously published results.[30,35]

The surface coverages ($\Gamma$) of RuC on the FTO|t-$TiO_2$ films were quantified using the reported equation $\Gamma = A/\varepsilon$,[36] where $A$ represents the absorption intensity of FTO|t-$TiO_2$ |RuC and $\varepsilon$ is the molar extinction efficiency ($\varepsilon_{RuC}$ = 10 392 $cm^{-1}$ $M^{-1}$, see Figure S2). The absorption changes of RuC on the FTO|t-$TiO_2$ film were monitored at 463 nm. In Figure 3c, the saturated surface coverages RuC on FTO|1-$TiO_2$, FTO|2-$TiO_2$, and FTO|3.5-$TiO_2$ are 3.51, 7.70, and 15.4 × $10^{-9}$ mol $cm^{-2}$, respectively, suggesting that the surface coverage enhanced linearly with the increase in the thickness of FTO|t-$TiO_2$ films. We assume that surface defect sites and/or porous sites would be increased with the thicker $TiO_2$ NRA because the more randomly oriented vertical alignment of the thicker $TiO_2$ NRA occurs.[25] RuC dye solution would fill in surface defect and/or porous sites, resulting in increased pore filling, which is defined as the pore volume fraction occupied by the RuC. When pore filling for the thicker $TiO_2$ NRA is increased, surface coverage also increases.[37] Moreover, FTO|1-$TiO_2$ was chosen to monitor the adsorption and emission of RuC onto the surface of $TiO_2$ NRAs from acetonitrile (ACN) solution (Figure S3a, b). The surface coverage of FTO|1-$TiO_2$|RuC is plotted as a function of time (Figure S3c). The photocatalyst RuC coverage on the film increases with time and saturates after 3 h without shifting the maximum wavelengths in the excitation and emission spectra. Note that the adsorption rate of the photocatalyst RuC on the FTO|1-$TiO_2$ is similar to that of RuC on the typical meso-$TiO_2$ films with a thickness of ~12 $\mu$m according to our previous study.[36] However, the surface coverage of RuC on the FTO|1-$TiO_2$ is lower at saturation as compared with a surface coverage of ~5.0 × $10^{-8}$ mol $cm^{-2}$ for RuC on a 12 $\mu$m thick meso-$TiO_2$ film.

Langmuir isotherm experiments were performed to calculate the adsorption constants with FTO|1-$TiO_2$|RuC, FTO|2-$TiO_2$|RuC, and FTO|3.5-$TiO_2$|RuC as shown in Figure S4. The Langmuir isotherm model assumed that (i) a monolayer coverage is reached at saturation, (ii) there is no interaction between adsorbates, and (iii) all adsorption surface is available to all adsorbates.[38,39] According to this model, the three-electrode types follow the trend of increasing adsorption constants from 0.07, 0.66, to 1.26 × $10^6$ $M^{-1}$, following the sequence FTO|3.5-$TiO_2$|RuC (3.5 $\mu$m long $TiO_2$ NR) < FTO|2-$TiO_2$|RuC (2 $\mu$m long $TiO_2$ NR) < FTO|1-$TiO_2$|RuC (1 $\mu$m long $TiO_2$ NR). This increase in adsorption constant with thinner $TiO_2$ NR indicates that the RuC molecules have much stronger interactions with the FTO|1-$TiO_2$ film, revealing a


https://doi.org/10.1021/acsami.1c20795
ACS Appl. Mater. Interfaces 2022, 14, 22799−22809

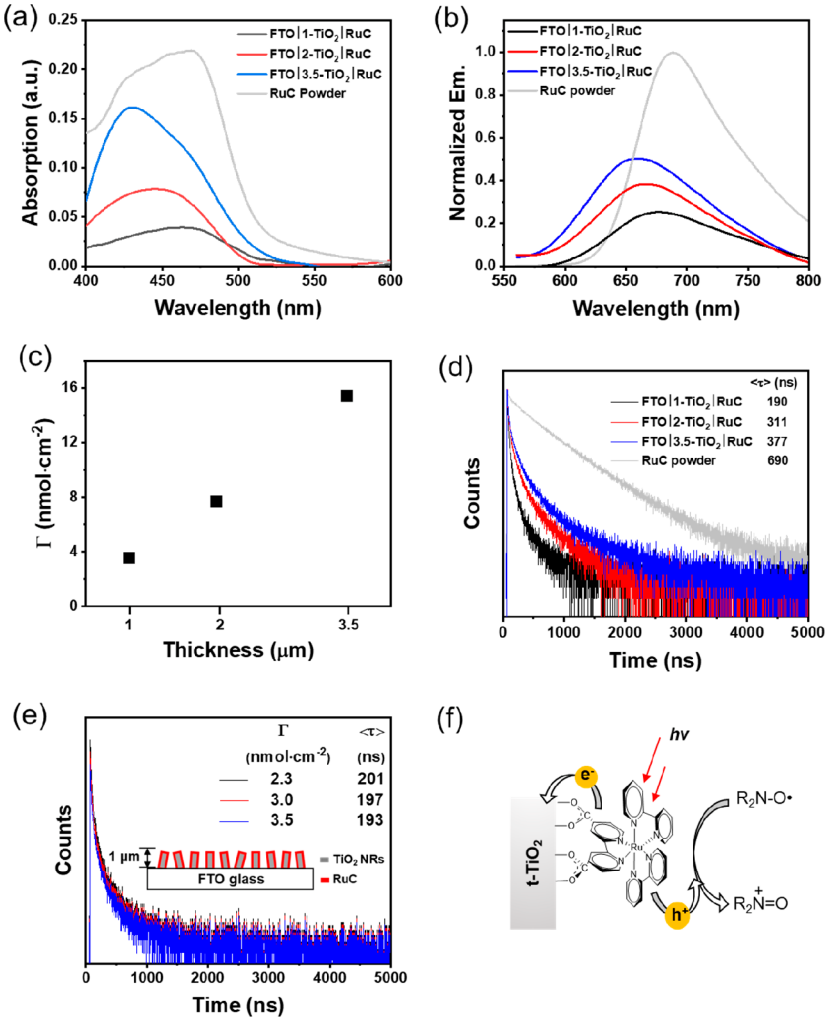


**Figure 3.** (a) UV−vis absorption and (b) emission spectra of RuC powder (gray) and FTO|t-$TiO_2$|RuC films, $t$ = 1 (black), 2 (red), and 3.5 $\mu$m (blue). Emission spectra obtained with excitation at $\lambda_{ex}$ = 450 nm. (c) Surface coverage plots of RuC on FTO|t-$TiO_2$ ($t$ = 1, 2, and 3.5 $\mu$m). (d) Time-resolved emission for RuC power and FTO|t-$TiO_2$|RuC ($t$ = 1, 2, and 3.5 $\mu$m). (e) Time-resolved emission for FTO|1-$TiO_2$|RuC with the surface coverage of 2.3, 3.0, and 3.5 nmol $cm^{-2}$. (Inset: the average lifetimes of FTO|1-$TiO_2$|RuC with the surface coverage of 2.3, 3.0, and 3.5 nmol $cm^{-2}$ are shown.) The decays are fit to a triexponential function, with time constants and amplitudes listed in Tables S2 and S3. (f) Illustration of the t-$TiO_2$, RuC, and ACT components of the photoanode.

more homogeneous coating of RuC onto the FTO|1-$TiO_2$|RuC surface as compared to the longer $TiO_2$ NRAs. In contrast, this lower adsorption constant for FTO|3.5-$TiO_2$|RuC was shown. Our rationalization is that after the formation of monolayer coverage for the thicker $TiO_2$ films (2 or 3.5 $\mu$m), the RuC molecules can be congregated or trapped into defect and/or porous sites, leading to weaker binding interaction between the RuC and nonporous $TiO_2$ surface (the schematic illustration is shown in Figure S5). Thus, despite the high value of the maximum surface coverages for the thicker films, the decreased adsorption binding constants are obtained in this work. For the FTO|1-$TiO_2$|RuC films, the RuC molecules are homogeneously anchored to a nonporous $TiO_2$ surface followed by monolayer coverage of RuC on the surface of $TiO_2$ at saturation, leading to the highest adsorption constant.

Furthermore, as shown in Figure 3d, the weighted average lifetimes $\langle\tau\rangle$ for the photoexcited RuC* on the FTO|1-$TiO_2$|RuC, FTO|2-$TiO_2$|RuC, and FTO|3.5-$TiO_2$|RuC films showed significant emission quenching with $\langle\tau\rangle$ = 190, 311, and 377 ns, respectively, in comparison to the lifetime of the RuC powder ($\langle\tau\rangle$ = 690 ns). The decrease in excited-state lifetime for RuC* indicates efficient quenching of the $TiO_2$ NRA, with the largest decrease observed for FTO|1-$TiO_2$. To develop an understanding of the interfacial dynamics of RuC at FTO|t-$TiO_2$, we chose the FTO|1-$TiO_2$|RuC films and measured the lifetimes at different loading levels as controlled by the soak time in the RuC solution. Deposition times of 0.5, 2, and 4 h gave calculated surface coverages for FTO|1-$TiO_2$|RuC of 2.25, 2.99, and 3.51 nmol $cm^{-2}$, respectively. Interestingly, in Figure 3e, as the RuC loading increased, the emission decay slightly accelerated to 201, 197, and 193 ns for the surface coverages of 2.3, 3.0, and 3.5 nmol $cm^{-2}$ for FTO|1-$TiO_2$|RuC, respectively. In other words, the lifetimes of the FTO|1-$TiO_2$|RuC decreased slightly with the increase in surface coverage of RuC on the 1 $\mu$m $TiO_2$ NRA. More importantly, in contrast, the lifetimes of the FTO|t-$TiO_2$|RuC increased as the surface coverages (or nanorod thickness) increased on basis of the above observation. The key assumption made on the basis of the photophysical experiments including UV−vis absorption and emission lifetime measurements is that RuC can be more homogeneously coated onto the shorter nanorods, especially


https://doi.org/10.1021/acsami.1c20795
ACS Appl. Mater. Interfaces 2022, 14, 22799−22809

FTO|1-$TiO_2$, as compared to the longer $TiO_2$ NRA surfaces. Because of this, more efficient excited-state quenching arising from electron injection by photoexcited RuC* occurs with the shorter $TiO_2$ nanorod interfaces. Maximum absorption, emission, surface coverage, adsorption constants, and excited-state lifetimes for the RuC powder and FTO|t-$TiO_2$|RuC (t = 1, 2, 3.5 $\mu$m) films are summarized in Table 1. Taken together,

**Table 1. Photophysical Properties and Surface Coverages of RuC Powder and FTO|t-$TiO_2$|RuC ($t$ = 1, 2, 3.5 $\mu$m)**

| | $\lambda_{abs}$, (nm) | $\lambda_{em}$, (nm) | $\Gamma$ (nmol $cm^{-2}$) | $K_{ad}$ ($\times 10^6$, $M^{-1}$) | $\tau_{avg}$ (ns) |
|---|---|---|---|---|---|
| RuC powder | 465 | 689 | | | 690 |
| FTO\|1-$TiO_2$\| RuC | 463 | 675 | 3.51 | 1.26 | 190 |
| FTO\|2-$TiO_2$\| RuC | 445 | 667 | 7.70 | 0.66 | 311 |
| FTO\|3.5-$TiO_2$\| RuC | 430 | 659 | 15.40 | 0.07 | 377 |

the quenching of surface-immobilized RuC* by t-$TiO_2$ under the visible-light illumination suggested clear evidence for electron transfer that can support visible-light-driven oxidation of the $R_2N-O\bullet$ (ACT) radical to form the $R_2N^+=O$ (the oxidized ACT form) as shown in Figure 3f. The oxidized ACT species serves as the strong oxidizing agent to carry out aliphatic and/or benzylic oxidation.[40]

The photocurrent responses of the three FTO|t-$TiO_2$|RuC electrodes in a DSPEC were examined in the presence of ACT. Figure 4a and 4b show the photocurrent transients in the absence and presence of ACT with an applied bias of 0.45 V vs SCE during on/off cycles of the incident AM1.5G illumination (1 sun, 100 mW $cm^{-2}$). In Figure 4a, upon illumination in the absence of ACT, the photoanodic currents from the FTO|t-$TiO_2$|RuC films decayed immediately for the initial 15 s and stabilized at 14−31 $\mu$A·$cm^{-2}$. These high initial anodic spikes followed by a rapid decay of the photocurrent have been observed in previous DSPEC studies.[7,41,42] Figure 4b exhibits the photocurrent transients of the FTO|t-$TiO_2$|RuC films in the presence of ACT. The three FTO|t-$TiO_2$|RuC films coupled with 2.5 mM ACT resulted in a significant increase of steady photocurrents compared to the absence of ACT, indicating that the aminoxyl radical can effectively regenerate the ground-state RuC(II) following photoexcited electron injection of RuC(II)* to $TiO_2$.[30] Furthermore, the photocurrent transients at the FTO|1-$TiO_2$|RuC, FTO|2-$TiO_2$|RuC, and FTO|3.5-$TiO_2$|RuC with ACT showed steady anodic currents of 380, 180, and 70 $\mu$A $cm^{-2}$, respectively. This result revealed that FTO|1-$TiO_2$|RuC can be effective at driving alcohol oxidation when coupled with the presence of ACT in the ACN solution. Incident photon-to-current efficiency (IPCE) measurements were performed with the FTO|t-$TiO_2$ electrodes before and after the immobilization of RuC as shown in Figure 4c. The IPCE spectra of the FTO|1-$TiO_2$|RuC, FTO|2-$TiO_2$|RuC, and FTO|3.5-$TiO_2$|RuC showed a maximum value of 9, 4, and 3%, respectively, at ∼460 nm that related to the MLCT absorption band of the RuC. A FTO|1-$TiO_2$ film without RuC did not show photocurrent response over illuminated wavelength range showing the light response of the surface was due to the adsorbed RuC. We expected that increased surface coverages for the longer $TiO_2$ NRA surfaces would give higher IPCE results. However, the FTO|1-$TiO_2$|RuC film with the lowest surface coverage exhibited the largest

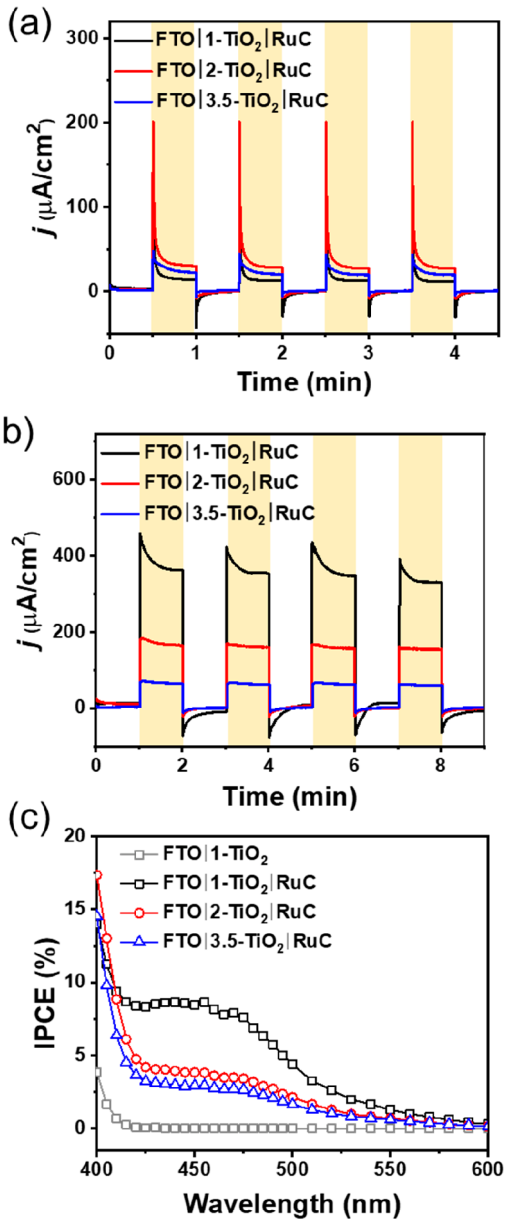


**Figure 4.** Photocurrent−time traces measured with light on/off cycles for (a) the FTO|t-$TiO_2$ |RuC electrode in 0.1 M $TBAPF_6$ acetonitrile solution and for (b) FTO|t-$TiO_2$|RuC electrodes as the same electrolyte with the addition of ACT (2.5 mM) with an applied bias of 0.45 V vs SCE under AM1.5G illumination. (c) Incident photon-to-current efficiency (IPCE) spectra of a FTO|1-$TiO_2$ electrode (gray diamond) and FTO|t-$TiO_2$|RuC electrodes ($t$ = 1 (black square), 2 (red circle), 3 $\mu$m (blue triangle)).

IPCE values under the conditions studied. This result reinforces those above and shows that electron injection is less efficient with thicker $TiO_2$ NRA surfaces.

To further understand the charge transfer process at the photoelectrodes, we carried out electrochemical impedance spectroscopy (EIS) for the FTO|1-$TiO_2$|RuC, FTO|2-$TiO_2$|RuC, and FTO|3.5-$TiO_2$|RuC electrodes. The EIS spectra were fitted by adopting the equivalent circuit[43] as presented in Figure 5a (inset). The charge transfer and recombination resistance ($R_{ct}$), and chemical capacitance ($Z_{CPE}$) values are summarized in Table S4. Overall, FTO|1-$TiO_2$|RuC showed the smallest values for $R_{ct}$ and $Z_{CPE}$, indicating more facile


https://doi.org/10.1021/acsami.1c20795
ACS Appl. Mater. Interfaces 2022, 14, 22799−22809

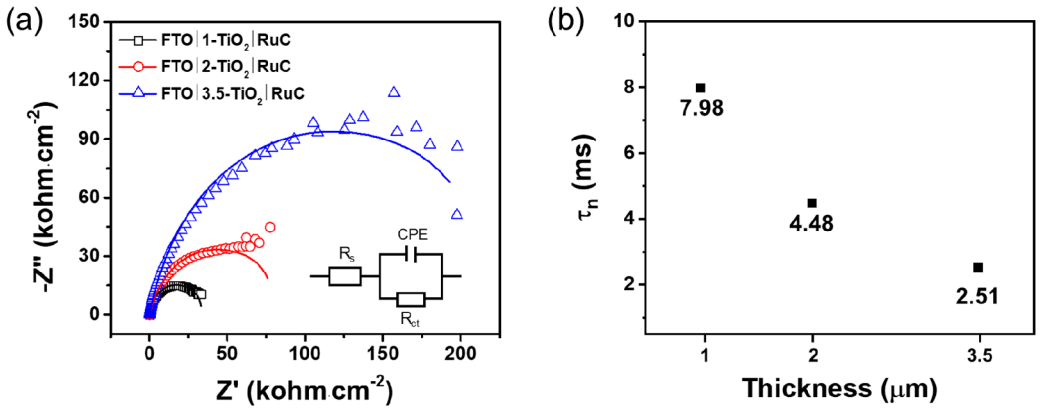


**Figure 5.** (a) Nyquist plots for the FTO|t-$TiO_2$|RuC measured in the dark. The inset displays an equivalent circuit of DSPECs. (b) Electron lifetimes, $\tau_n$, of FTO|t-$TiO_2$|RuC, derived from the EIS bode plots.

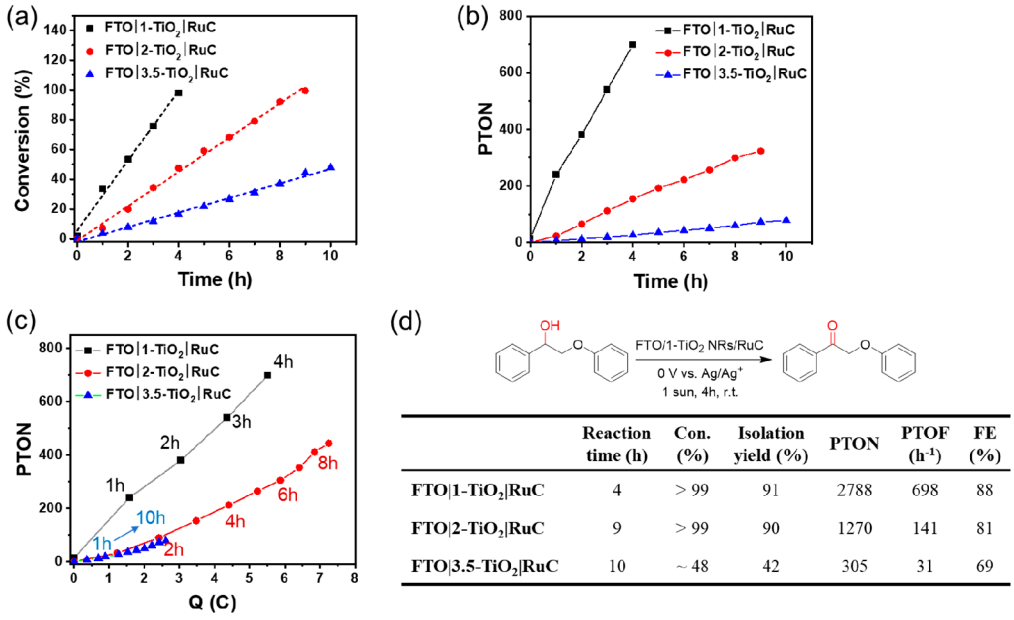


| | Reaction time (h) | Con. (%) | Isolation yield (%) | PTON | PTOF ($h^{-1}$) | FE (%) |
|---|---|---|---|---|---|---|
| FTO\|1-$TiO_2$\|RuC | 4 | > 99 | 91 | 2788 | 698 | 88 |
| FTO\|2-$TiO_2$\|RuC | 9 | > 99 | 90 | 1270 | 141 | 81 |
| FTO\|3.5-$TiO_2$\|RuC | 10 | ~ 48 | 42 | 305 | 31 | 69 |

**Figure 6.** (a) Conversion efficiency and (b) PTON plot as a function of time for the photocatalytic oxidation of PP-OH to PP-CHO using FTO|t-$TiO_2$|RuC photoanodes with ACT under an applied bias of 0.35 V vs SCE at room temperature. (d) Summary of reaction time, conversion efficiency, isolation yield, PTON, PTOF, and Faradaic efficiency for the FTO|t-$TiO_2$|RuC photoanodes with ACT.

electron transfer with the thinner $TiO_2$ NRAs. The diameter of the semicircle component of the Nyquist plots for FTO|t-$TiO_2$|RuC ($t$ = 1, 2, 3.5 $\mu$m), which is related to $R_{ct}$ and the surface electron transfer process,[44,45] is the smallest for FTO|1-$TiO_2$|RuC. The smaller $R_{ct}$ suggests better interaction with the electrolyte, which would support enhanced photocatalytic activity for benzylic alcohol oxidation at photoanode. The electron lifetimes ($\tau_n$) of FTO|t-$TiO_2$|RuC films were calculated using eq 1:[46,47]

$$\tau_n = \frac{1}{2\pi f_{max}} \quad (1)$$

where $f_{max}$ is the frequency at which the phase angle reaches the maximum in the bode plots of the EIS test (Figure S6). The maximum frequencies of for FTO|t-$TiO_2$|RuC films and the derived electron lifetimes are summarized in Table S5. Electron lifetime is a critical parameter that is related to the time an electron lasts following interfacial charge separation. As shown in Figure 5b, the electron lifetime in FTO|t-$TiO_2$|RuC films decreases in the order of FTO|1-$TiO_2$|RuC (7.98 ms) > FTO|2-$TiO_2$|RuC (4.48 ms) < FTO|3.5-$TiO_2$|RuC (2.51 ms). The $\tau_n$ increases nearly 3.2-fold for FTO|1-$TiO_2$|RuC compared to that of FTO|3.5-$TiO_2$|RuC. This is clear evidence that charge transfer is much faster on a thinner FTO|t-$TiO_2$ film, with less charge recombination, allowing for enhancement of the photocatalytic performance.

The FTO|t-$TiO_2$|RuC films were investigated as DSPEC photoanodes to drive photocatalytic oxidation of the $C_\alpha$–OH in PP-OH. The conditions studied consisted of 2.5 mM ACT present in the acetonitrile electrolyte, AM1.5G illumination (100 mW $cm^{-2}$), and an applied bias of 0.35 V vs SCE. The formation of the ketone (PP-CHO) from the starting PP-OH was monitored by gas chromatography (GC-FID) with retention times of 17.94 min for PP-CHO (Figure S7). The yield of the PP-CHO product was evaluated and confirmed by $^1$H NMR and GC-MS with DMSO as an internal standard (Figure S8). In Figure 6a, the photocatalytic conversion of PP-OH to PP-CHO was complete (yield >99%) after the 4 and 9 h of continuous illumination for the FTO|1-$TiO_2$|RuC and FTO|2-$TiO_2$|RuC, respectively. Only ~50% conversion of PP-


https://doi.org/10.1021/acsami.1c20795
ACS Appl. Mater. Interfaces 2022, 14, 22799–22809

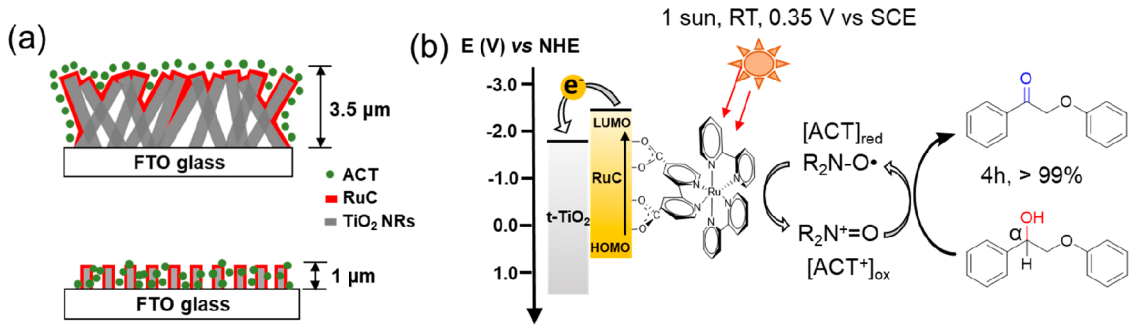


**Figure 7.** (a) Schematic illustration of the effect of $TiO_2$ NR thickness. (b) Proposed mechanism of a 1D 1-$TiO_2$ NR type DSPEC with RuC and ACT for photocatalytic oxidation of the PP-OH.

OH to PP-CHO was observed after 10 h for FTO|3.5-$TiO_2$|RuC. As anticipated by the photophysical and IPCE results, FTO|1-$TiO_2$|RuC in the presence of ACT showed the best photocatalytic activity. To characterize the photocatalytic activity of RuC with the FTO|t-$TiO_2$|RuC photoanodes, we obtained the photocatalytic turnover number (PTON) by dividing the mole of PP-CHO product by the mole of RuC anchored to the surface of the FTO|t-$TiO_2$ (eq 2).

$$\text{PTON} = \frac{\text{moles of product}}{\text{moles of RuC on the surface}} \tag{2}$$

As shown in Figure 6b, the PTON number is linearly correlated to the reaction time, indicating a constant conversion rate of PP-OH to PP-CHO during the illumination period. The maximum PTON values of FTO|1-$TiO_2$|RuC, FTO|2-$TiO_2$|RuC, and FTO|3.5-$TiO_2$|RuC were 2788, 1270, and 305 for time points of 4, 9, and 10 h, respectively. According to the long-term photocurrent of FTO|t-$TiO_2$|RuC photoanodes (Figure S9a), the total consumed charges ($Q$) of FTO|t-$TiO_2$|RuC over the continuous 10 h illumination were evaluated using the equation $Q = I{\cdot}t$, where $I$ represents for photocurrent and $t$ stands for reaction time. Plots of $Q$ as a function of time are shown in Figure S9b. It is also worth noting that we observed the decay of photocurrent over continuous 10 h of illumination. We assume that oxidized or decomposed ACT in the presence of PP-OH would not be completely regenerated to the original ACT form resulting in the photocurrent decay, and this is consistent with our previous study.[30] This result reinforces those above and shows that electron injection is less efficient with thicker $TiO_2$ NRA surfaces. Furthermore, the photocatalytic stability in a DSPEC is an important factor for the photocatalytic oxidation of benzyl alcohol. The photostability for FTO|1-$TiO_2$|RuC with 0.1 M $TBAPF_6$ and 2.5 mM ACT in ACN was carried out before and after AM1.5G illumination over 10 h of continuous illumination at room temperature. Figure S10 shows the UV−vis absorption spectrum before and after 10 h of AM 1.5G illumination. The MLCT absorption band from RuC from FTO|1-$TiO_2$|RuC was slightly reduced compared to the MLCT absorption band before the illumination. This result indicates no substantial change in the absorption features for RuC and indicates that there was no significant desorption or decomposition of RuC in ACN, which is consistent with our recent photostability test for RuC-coated $TiO_2$ nanoparticles.[48]

Performing this analysis revealed a Faradaic efficiency (FE) of 88, 81, and 69% at 4, 9, and 10 h for the FTO|1-$TiO_2$|RuC, FTO|2-$TiO_2$|RuC, and FTO|3.5-$TiO_2$|RuC, respectively, according to eq 3, where $n$ is the moles, $Z$ is charge passed, and $F$ is the Faraday constant in $C{\cdot}mol^{-1}$.

$$\text{FE}(\%) = \frac{nZF}{Q} \tag{3}$$

$$\text{PTOF}\ (h^{-1}) = \frac{\text{PTON}}{\text{reaction time (h)}} \tag{4}$$

Furthermore, the consumed charges for all the FTO|t-$TiO_2$|RuC electrodes are linearly proportional to the PTON as shown in Figure 6c. The reaction time, the conversion efficiency, PTON, the photocatalytic turnover frequency (PTOF, eq 4), and the FE for the photocatalytic oxidation of PP-CHO are listed in Figure 6d. These results reveal that the well-ordered FTO|1-$TiO_2$|RuC (with the shortest vertical height) showed the maximum photocatalytic efficiency with an excellent conversion yield, isolation yield, PTON, and PTOF for the benzylic alcohol oxidation under 1 sun illumination with the minimal applied bias at room temperature. These results reveal that the well-ordered FTO|1-$TiO_2$|RuC (with the shortest vertical height) showed enhanced photocatalytic efficiency with an excellent conversion yield, PTON, and PTOF for the oxidation of benzylic alcohol.

We hypothesize that the photocatalyst RuC shows more dense loading at the longer $TiO_2$ NRA electrodes. This combined with the less vertical alignment of these surfaces gives more limited accessibility of ACT at the interface of the RuC-coated $TiO_2$ NRA electrode. According to the previous study, the performance of longer $TiO_2$ NRAs can be attributed to the randomly oriented vertical alignment of the rods comprising the surface.[25] Furthermore, the RuC can achieve more homogeneous coatings on the surface of the shorter $TiO_2$ NRAs, which enables enhanced permeability for ACT molecules to diffuse deep into the film surface (Figure 7a). This results in higher photocurrent density and IPCE results, leading to better photocatalytic oxidation efficiency for benzylic alcohol oxidation in a DSPEC system. Therefore, the selection of the $TiO_2$ NRA length is the key factor to consider in improving the DSPEC performance for photocatalytic oxidation of alcohols under mild conditions. According to previous studies,[14,49,50] an aminoxyl radical mediated alcohol oxidation mechanism has been well established. Taken together with this current study, we show a proposed mechanism for photocatalytic oxidation of the 2° benzyl alcohol in PP-OH in Figure 7b. The surface-bound RuC(II) on the FTO|1-$TiO_2$ substrate is excited under the 1 sun illumination followed by the formation of the excited-state RuC*. After photoexcited electron injection to the conduction


https://doi.org/10.1021/acsami.1c20795
ACS Appl. Mater. Interfaces 2022, 14, 22799−22809

band of $TiO_2$ NRA, the oxidized RuC(III) is generated at the surface of the $TiO_2$ ($e^-$) NRA. The ground state RuC(II) is then regenerated by the hole transfer from RuC(III) to the ACT ($R_2N-O\bullet$) radical species. Upon hole transfer, the oxoammonium $R_2N^+{=}O$ ($[ACT^+]_{ox}$) species, a strong oxidizing agent is generated. The reaction of 2 equiv. of $ACT^+$ with the $C_\alpha$ of PP-OH results in the production of 1 equiv. of the ketone, PP-CHO. The ACT equivalents are regenerated in this process and can repeat the sequential photophysical and chemical steps above. In a complete system, the 2 equiv. of $H^+$ generated from the oxidation of PP-OH would be reduced to form $H_2$ though the cathodic half-reaction of the full DSPEC, although this current work focuses only on the photoanode activity.[12,S1]

## CONCLUSION

We investigated the photoinduced process with well-ordered 1D vertically aligned rutile t-$TiO_2$ NR ($t$ = 1, 2, 3.5 $\mu$m) films sensitized by a carboxylic-acid-functionalized RuC photocatalyst. With ACT present in solution, these electrodes can drive the photocatalytic oxidation of a 2° benzylic alcohol in a lignin model compound, PP-OH. The FTO|1-$TiO_2$|RuC photoanodes incorporated with ACT demonstrated excellent conversion efficiency of >99% over 4 h with FE of 88% and PTON of ∼2800 under 1 sun illumination, at room temperature, and under the minimal applied bias. Photophysical and photoelectrochemical properties of FTO|t-$TiO_2$|RuC films shows that the photoexcited RuC on the 1D $TiO_2$ NRAs was more efficiently quenched by shorter nanorod lengths. This result indicated that the well-controlled nanostructure architecture with RuC and ACT in the DSPEC supports efficient intermolecular charge transfer under visible-light illumination and leads to enhanced photocatalytic oxidation of benzyl alcohol under mild conditions.

## EXPERIMENTAL SECTION

**Materials.** The bis(2,2′-bipyridine)(4,4′-dicarboxy-2,2′-bipyridine)Ru(II) hexafluorophosphate (RuC)[31,52] and 2-phenoxy-1-phenylethanol (PP-OH)[11,14] were prepared, and the structural analysis of RuC and PP-OH was performed using $^1H/^{13}C$ NMR and GC-MS described in the previously reported literature.[14,30] 4-Acetamide-2,2,6,6-tetramethylpiperidine 1-oxyl (ACT) and tetrabutylammonium hexafluorophosphate ($TBAPF_6$) were purchased from AK Scientific Inc. and used without further modification. Fluorine-doped tin oxide (FTO, TEC 15) substrates were purchased from Hartford Glass.

**Fabrication of FTO|t-$TiO_2$|RuC Photoanode.** The FTO|t-$TiO_2$ films were fabricated according to the previous hydrothermal method.[53,54] Titanium(IV) n-butoxide (0.969 g, 2.85 mmol) and sodium citrate dihydrate (0.566 g, 1.93 mmol) were added into a mixture of 36% HCl and water (50 mL, v:v = 1:1) and vigorously stirred for 1 h. FTO glass substrates were cleaned with soap and water, isopropanol, and acetone by sonication and dried with $N_2$ gas. The cleaned FTO substrates were then dipped into the above mixture solution of 30 mL in a steel-lined Teflon autoclave followed by heating at 135, 150, or 170 °C for the fabrication of FTO|1-$TiO_2$, FTO|2-$TiO_2$, or FTO|3.5-$TiO_2$ films, respectively, during a period of 14 h. The film was cooled at a rate of 10 °C per minute to room temperature and washed with ACN solvent. The film was then annealed by heating at 400 °C for 3 h under air. Upon cooling to room temperature, the FTO|t-$TiO_2$ films were obtained with lengths of 1 (135 °C), 2 (150 °C), and 3.5 (170 °C) $\mu$m, respectively. The FTO|t-$TiO_2$ film was immersed into the RuC solution (1.16 mM) in acetonitrile for 12 h at room temperature to prepare FTO|t-$TiO_2$|RuC films.

**Characterization Methods and Instrumentation.** A JEOL LTD JSM-7610F SEM was operated at an accelerating voltage of 10 kV to monitor FTO|t-$TiO_2$ and FTO|t-$TiO_2$|RuC films. UV−visible absorption spectra were obtained using a Thermo Scientific Evolution 220 UV−vis spectrometer. The spectra were obtained with a background of FTO|t-$TiO_2$ for the measurement of FTO|t-$TiO_2$|RuC films. The molar extinction coefficient ($\varepsilon$, $cm^{-1}$ $M^{-1}$) of RuC was calculated by plotting absorption intensity versus concentration via the Lambert−Beer Law eq 5:

$$A = \varepsilon l c \tag{5}$$

where $A$ is absorbance, $l$ is the length of the path light travel through the solution, and $c$ is the concentration of RuC. The surface coverages of RuC molecules ($\Gamma$) on the surface of FTO|t-$TiO_2$|RuC films were calculated using the eq 6:[30,55,56]

$$\Gamma = A/\varepsilon \tag{6}$$

where $A$ is the maximum absorbance of obtained FTO|t-$TiO_2$|RuC films, and $\varepsilon$ stands for the molar extinction coefficient of RuC in acetonitrile (in $cm^{-1}$ $M^{-1}$).

To investigate the adsorption isotherm, a set of FTO|t-$TiO_2$ ($t$ = 1, 2, and 3.5 $\mu$m) films were soaked in RuC solutions with varying concentrations (2, 5, 15, 30, 60, 120, and 240 $\mu$M) in ACN for 20 h. The UV−vis absorption spectra of the obtained FTO|t-$TiO_2$|RuC films were measured and the absorption values at 463 nm were recorded. The surface coverages ($\Gamma$) of RuC molecules on the films were calculated using eq 6. The Langmuir isotherm model is described as eq 7 and applied to the plots of the surface coverage versus RuC concentration according to the Langmuir isotherm equation:

$$\Gamma = \Gamma^{max}\frac{K_{ad}[M]}{1 + K_{ad}[M]} \tag{7}$$

where $\Gamma^{max}$ is the maximum absorbance of FTO|t-$TiO_2$|RuC films, $K_{ad}$ stands for the adsorption constant (in $M^{-1}$), and [M] is the concentration of RuC in ACN solutions.

Steady-state emission and fluorescence lifetime measurements were carried out using an Edinburgh FLS 980 steady-state and time-resolved emission spectrometer. RuC powder was placed in a quartz sampler holder. The FTO|t-$TiO_2$|RuC electrodes were located on a sample holder, which were at a 45° angle to the excitation light source and the detector. An optical filter, $\lambda_{cutoff}$ = 420 nm, was placed in front of the detector. The average emission lifetime obtained from time-resolved photoluminescence measurements were calculated using the following equation:

$$\langle\tau\rangle = \frac{\sum_{i=1}^{3}\alpha_i\tau_i^3}{\sum_{i=1}^{3}\alpha_i\tau_i} \tag{8}$$

where $\langle\tau\rangle$ is experimentally detected PL decay, $\alpha_i$ is the fractional amplitude of component $i$, and $\tau_i$ is the lifetime of component $i$.

Incident photon-to-current efficiency (IPCE) measurements were performed using a TLS-72-X300 science tech tunable light source. A single-component three-electrode cell with a platinum wire as the counter electrode, a FTO|t-$TiO_2$|RuC film as the working electrode and a nonaqueous $Ag/Ag^+$ quasi reference electrode was used. The 10 mL of ACN electrolyte contained 0.1 M $TBAPF_6$ and 2.5 mM ACT and was purged with nitrogen for 10 min prior to the start of an experiment. A constant nitrogen flow was kept over the head space during the measurements. Current was measured in 10 s light on and off periods at wavelength values between 600 and 400 nm. An applied bias of 0.15 V vs SCE was used for all IPCE experiments. A BBT-003 broadband thermopile detector (ScienceTech) was used to quantify the light intensity at each wavelength measured.

Photocurrent−time measurements were performed in a single-component three-electrode cell containing 0.1 M $TBAPF_6$ as the supporting electrolyte with the FTO|t-$TiO_2$|RuC photoanodes. The


https://doi.org/10.1021/acsami.1c20795
ACS Appl. Mater. Interfaces 2022, 14, 22799−22809

photoanode was illuminated using an LSH-7320 ABA LED solar simulator. The optical power density was adjusted to 100 mW $cm^{-2}$. The light on−off photocurrent measurements were taken by the FTO|t-$TiO_2$|RuC using a Versa STAT E2000 potentiostat with an applied voltage of 0.45 V vs SCE and 1 min interval in the presence and absence of 2.5 mM ACT. The potential of the $Ag/Ag^+$ quasi-reference electrode was calibrated with ferrocene/ferrocenium ($Fc/Fc^+$) as an external standard.

Electrochemical impedance spectroscopy (EIS) was obtained using a Gamry Interface 1010 E potential state. The active area of the FTO|t-$TiO_2$|RuC was 0.3 ± 0.05 $cm^2$. All measurements were performed using a single three-electrode component system in 0.1 M $TBAPF_6$ acetonitrile solution using an FTO|t-$TiO_2$|RuC working electrode, a $Ag/Ag^+$ reference electrode, and platinum counter electrode. The experimental parameters were 0.1 V DC voltage, 5 mV AC voltage, and the frequency range was 100 000 to 0.1 Hz.

Photocatalytic oxidative benzylic alcohol reactions were carried out using the same setup as the above experiments. PP-OH (5 mg, 0.023 mmol) and ACT (2.7 mg, 0.013 mmol) were dissolved in 5 mL of acetonitrile with 0.1 M $TBAPF_6$ as the supporting electrolyte in the DSPEC system. Under an applied voltage of 0.35 V vs SCE, the mixture was stirred under AM1.5G light illumination and the oxidative conversion of PP-OH to PP-CHO was monitored using GC-FID (Shimadzu 2010 GC). The quantification of cleavage products was achieved by GC-FID fitted with a 3 m × 0.25 mm i.d. capillary column with AOCI205 autosampler. Helium gas was used as a carrier gas and the GC-FID system was held at 65 °C for 3 min. The temperature was ramped from 65 to 300 °C with a heating rate of 10 °C $min^{-1}$ and held at 300 °C for 5 min. One hundred mictroliters of crude products from the reaction mixture were taken every hour and dried under vacuum. The dried crude products were then redissolved in chloroform for GC-FID measurements with the addition of the internal standard, DMSO (0.033 μL, 0.46 μmol).

$^1$H NMR analysis was conducted with PP-OH before and after photocatalytic conversion in the DSPEC. After the completion of photocatalytic reactions, the product was separated from the reaction mixture by precipitation in a 1:1 mixture of ethyl acetate and hexane. The obtained products were then dissolved in $CDCl_3$ for $^1$H NMR analysis. DMSO (0.6 μL, 8.4 μmol) was added into the mixture as an internal standard.

## ■ ASSOCIATED CONTENT

### Supporting Information

The Supporting Information is available free of charge at https://pubs.acs.org/doi/10.1021/acsami.1c20795.

Additional experimental details, characterizations, and methods; SEM image and surface profilometry of FTO|t-$TiO_2$, UV−vis absorption extinction, steady-state emission, adsorption isotherms and molar coefficient of RuC, time-resolved emission decay fits for RuC powder and FTO|t-$TiO_2$|RuC films; charge transfer and recombination resistance, chemical capacitance, mass transport resistance, long-term photocurrent, photostability of the FTO|t-$TiO_2$|RuC, GC-FID, and $^1$H NMR spectrum and GC-MS of PP-CHO (PDF)

## ■ AUTHOR INFORMATION


### Corresponding Author

**Gyu Leem** − *Department of Chemistry, State University of New York College of Environmental Science and Forestry, Syracuse, New York 13210, United States; The Michael M. Szwarc Polymer Research Institute, Syracuse, New York 13210, United States;* orcid.org/0000-0003-0169-1096; Email: gyleem@esf.edu

### Authors

**Shuya Li** − *Department of Chemistry, State University of New York College of Environmental Science and Forestry, Syracuse, New York 13210, United States*

**Eric Wolfgang Shuler** − *Department of Chemistry, State University of New York College of Environmental Science and Forestry, Syracuse, New York 13210, United States*

**Debora Willinger** − *Department of Chemistry and Biochemistry, College of Science and Engineering, Texas Christian University, Fort Worth, Texas 76129, United States*

**Hai Tien Nguyen** − *Department of Chemistry, State University of New York College of Environmental Science and Forestry, Syracuse, New York 13210, United States*

**Saerona Kim** − *Department of Chemistry, State University of New York College of Environmental Science and Forestry, Syracuse, New York 13210, United States*

**Hyeong Cheol Kang** − *Department of Energy and Materials Engineering, Research Center for Photoenergy Harvesting & Conversion Technology (phct), Dongguk University, Seoul 04620, Republic of Korea*

**Jae-Joon Lee** − *Department of Energy and Materials Engineering, Research Center for Photoenergy Harvesting & Conversion Technology (phct), Dongguk University, Seoul 04620, Republic of Korea;* orcid.org/0000-0001-8966-0336

**Weiwei Zheng** − *Department of Chemistry, Syracuse University, Syracuse, New York 13244, United States;* orcid.org/0000-0003-1394-1806

**Chang Geun Yoo** − *Department of Chemical Engineering, State University of New York College of Environmental Science and Forestry, Syracuse, New York 13210, United States; The Michael M. Szwarc Polymer Research Institute, Syracuse, New York 13210, United States;* orcid.org/0000-0002-6179-2414

**Benjamin D. Sherman** − *Department of Chemistry and Biochemistry, College of Science and Engineering, Texas Christian University, Fort Worth, Texas 76129, United States;* orcid.org/0000-0001-9571-5065

Complete contact information is available at: https://pubs.acs.org/10.1021/acsami.1c20795


### Notes

The authors declare no competing financial interest.

## ■ ACKNOWLEDGMENTS

This work is supported by the USDA National Institute of Food and Agriculture, McIntire Stennis Program project (1023017, NYZ1161219). W.Z. acknowledges support from an NSF CAREER grant (Award CHE-1944978), an NSF IUCRC Phase I grant (Award 2052611), and a Syracuse University CUSE Grant (SD-10-2020). B.D.S. thank the Welch Foundation for support of this work through Award P-2044-20200401. J.-J.L. acknowledges support from the Korean National Research Foundation, funded by the Ministry of Science, ICT & Future Planning (Grant NRF-2021R1A2C2094554).

## ■ REFERENCES

(1) Luo, H.; Song, W.; Hoertz, P. G.; Hanson, K.; Ghosh, R.; Rangan, S.; Brennaman, M. K.; Concepcion, J. J.; Binstead, R. A.; Bartynski, R. A.; Lopez, R.; Meyer, T. J. A Sensitized $Nb_2O_5$

Photoanode for Hydrogen Production in a Dye-Sensitized Photoelectrosynthesis. *Cell. Chem. of Mater.* **2013**, *25*, 122−131.
(2) Sherman, B. D.; McMillan, N. K.; Willinger, D.; Leem, G. Sustainable Hydrogen Production from Water Using Tandem Dye-Sensitized Photoelectrochemical Cells. *Nano Converg.* **2021**, *8*, 7.
(3) Sherman, B. D.; Sheridan, M. V.; Wee, K.-R.; Marquard, S. L.; Wang, D.; Alibabaei, L.; Ashford, D. L.; Meyer, T. J. A Dye-Sensitized Photoelectrochemical Tandem Cell for Light Driven Hydrogen Production from Water. *J. Am. Chem. Soc.* **2016**, *138*, 16745−16753.
(4) Brennaman, M. K.; Dillon, R. J.; Alibabaei, L.; Gish, M. K.; Dares, C. J.; Ashford, D. L.; House, R. L.; Meyer, G. J.; Papanikolas, J. M.; Meyer, T. J. Finding the Way to Solar Fuels with Dye-Sensitized Photoelectrosynthesis Cells. *J. Am. Chem. Soc.* **2016**, *138*, 13085−13102.
(5) Jiang, J.; Sherman, B. D.; Zhao, Y.; He, R.; Ghiviriga, I.; Alibabaei, L.; Meyer, T. J.; Leem, G.; Schanze, K. S. Polymer Chromophore-Catalyst Assembly for Solar Fuel Generation. *ACS Appl. Mater. Interfaces* **2017**, *9*, 19529−19534.
(6) Leem, G.; Black, H. T.; Shan, B.; Bantang, J. P. O.; Meyer, T. J.; Reynolds, J. R.; Schanze, K. S. Photocathode Chromophore−Catalyst Assembly via Layer-By-Layer Deposition of a Low Band-Gap Isoindigo Conjugated Polyelectrolyte. *ACS Appl. Energy Materials* **2018**, *1*, 62−67.
(7) Leem, G.; Sherman, B. D.; Burnett, A. J.; Morseth, Z. A.; Wee, K.-R.; Papanikolas, J. M.; Meyer, T. J.; Schanze, K. S. Light-Driven Water Oxidation Using Polyelectrolyte Layer-by-Layer Chromophore−Catalyst Assemblies. *ACS Energy Lett.* **2016**, *1*, 339−343.
(8) Zhang, B.; Sun, L. Artificial Photosynthesis: Opportunities and Challenges of Molecular Catalysts. *Chem. Soc. Rev.* **2019**, *48*, 2216−2264.
(9) Zhu, Y.; Wang, D.; Huang, Q.; Du, J.; Sun, L.; Li, F.; Meyer, T. J. Stabilization of A Molecular Water Oxidation Catalyst on A Dye−Sensitized Photoanode by A Pyridyl Anchor. *Nat. Commun.* **2020**, *11*, 4610.
(10) Song, W.; Vannucci, A. K.; Farnum, B. H.; Lapides, A. M.; Brennaman, M. K.; Kalanyan, B.; Alibabaei, L.; Concepcion, J. J.; Losego, M. D.; Parsons, G. N.; Meyer, T. J. Visible Light Driven Benzyl Alcohol Dehydrogenation in a Dye-Sensitized Photoelectrosynthesis Cell. *J. Am. Chem. Soc.* **2014**, *136*, 9773−9779.
(11) Nikoloudakis, E.; Pati, P. B.; Charalambidis, G.; Budkina, D. S.; Diring, S.; Planchat, A.; Jacquemin, D.; Vauthey, E.; Coutsolelos, A. G.; Odobel, F. Dye-Sensitized Photoelectrosynthesis Cells for Benzyl Alcohol Oxidation Using a Zinc Porphyrin Sensitizer and TEMPO Catalyst. *ACS Catal.* **2021**, *11*, 12075−12086.
(12) Davis, K. A.; Yoo, S.; Shuler, E. W.; Sherman, B. D.; Lee, S.; Leem, G. Photocatalytic Hydrogen Evolution from Biomass Conversion. *Nano Converg.* **2021**, *8*, 6.
(13) Wu, X.; Fan, X.; Xie, S.; Lin, J.; Cheng, J.; Zhang, Q.; Chen, L.; Wang, Y. Solar Energy-Driven Lignin-First Approach to Full Utilization of Lignocellulosic Biomass under Mild Conditions. *Nat. Catal.* **2018**, *1*, 772−780.
(14) Li, S.; Li, Z.-J.; Yu, H.; Sytu, M. R.; Wang, Y.; Beeri, D.; Zheng, W.; Sherman, B. D.; Yoo, C. G.; Leem, G. Solar-Driven Lignin Oxidation via Hydrogen Atom Transfer with a Dye-Sensitized $TiO_2$ Photoanode. *ACS Energy Lett.* **2020**, *5*, 777−784.
(15) Wu, W.; Dutta, T.; Varman, A. M.; Eudes, A.; Manalansan, B.; Loqué, D.; Singh, S. Lignin Valorization: Two Hybrid Biochemical Routes for the Conversion of Polymeric Lignin into Value-added Chemicals. *Sci. Rep.* **2017**, *7*, 8420.
(16) Nguyen, J. D.; Matsuura, B. S.; Stephenson, C. R. J. A Photochemical Strategy for Lignin Degradation at Room Temperature. *J. Am. Chem. Soc.* **2014**, *136*, 1218−1221.
(17) Gazi, S.; Hung Ng, W. K.; Ganguly, R.; Putra Moeljadi, A. M.; Hirao, H.; Soo, H. S. Selective Photocatalytic C−C Bond Cleavage under Ambient Conditions with Earth Abundant Vanadium Complexes. *Chem. Sci.* **2015**, *6*, 7130−7142.
(18) Bosque, I.; Magallanes, G.; Rigoulet, M.; Kärkäs, M. D.; Stephenson, C. R. J. Redox Catalysis Facilitates Lignin Depolymerization. *ACS Cent. Sci.* **2017**, *3*, 621−628.
(19) Han, G.; Yan, T.; Zhang, W.; Zhang, Y. C.; Lee, D. Y.; Cao, Z.; Sun, Y. Highly Selective Photocatalytic Valorization of Lignin Model Compounds Using Ultrathin Metal/CdS. *ACS Catal.* **2019**, *9*, 11341−11349.
(20) Li, S.; Davis, K.; Leem, G. In *Lignin Utilization Strategies: From Processing to Applications*; American Chemical Society: Washington, D.C., 2021; Vol. *1377*, pp 97−121.
(21) Shiraishi, T.; Takano, T.; Kamitakahara, H.; Nakatsubo, F. Studies on Electro-Oxidation of Lignin and Lignin Model Compounds. Part 2: N-Hydroxyphthalimide (NHPI)-Mediated Indirect Electro-Oxidation of Non-Phenolic Lignin Model Compounds. *Holzforschung* **2012**, *66*, 311−315.
(22) Rahimi, A.; Azarpira, A.; Kim, H.; Ralph, J.; Stahl, S. S. Chemoselective Metal-Free Aerobic Alcohol Oxidation in Lignin. *J. Am. Chem. Soc.* **2013**, *135*, 6415−6418.
(23) Wang, M.; Lu, J.; Zhang, X.; Li, L.; Li, H.; Luo, N.; Wang, F. Two-Step, Catalytic C−C Bond Oxidative Cleavage Process Converts Lignin Models and Extracts to Aromatic Acids. *ACS Catal.* **2016**, *6*, 6086−6090.
(24) Pho, T. V.; Sheridan, M. V.; Morseth, Z. A.; Sherman, B. D.; Meyer, T. J.; Papanikolas, J. M.; Schanze, K. S.; Reynolds, J. R. Efficient Light-Driven Oxidation of Alcohols Using an Organic Chromophore−Catalyst Assembly Anchored to TiO2. *ACS Appl. Mater. Interfaces* **2016**, *8*, 9125−9133.
(25) Kim, H.-S.; Lee, J.-W.; Yantara, N.; Boix, P. P.; Kulkarni, S. A.; Mhaisalkar, S.; Grätzel, M.; Park, N.-G. High Efficiency Solid-State Sensitized Solar Cell-Based on Submicrometer Rutile $TiO_2$ Nanorod and $CH_3NH_3PbI_3$ Perovskite Sensitizer. *Nano Lett.* **2013**, *13*, 2412−2417.
(26) Zeman, C. J.; Kim, S.; Zhang, F.; Schanze, K. S. Direct Observation of the Reduction of Aryl Halides by a Photoexcited Perylene Diimide Radical Anion. *J. Am. Chem. Soc.* **2020**, *142*, 2204−2207.
(27) Li, S.; Hao, Z.; Wang, K.; Tong, M.; Yang, Y.; Jiang, H.; Xiao, Y.; Zhang, F. Visible Light-Enabled Selective Depolymerization of Oxidized Lignin by an Organic Photocatalyst. *Chem. Commun.* **2020**, *56*, 11243−11246.
(28) Leem, G.; Morseth, Z. A.; Puodziukynaite, E.; Jiang, J.; Fang, Z.; Gilligan, A. T.; Reynolds, J. R.; Papanikolas, J. M.; Schanze, K. S. Light Harvesting and Charge Separation in a $\pi$-Conjugated Antenna Polymer Bound to $TiO_2$. *J. Phys. Chem. C* **2014**, *118*, 28535−28541.
(29) Leem, G.; Sherman, B. D.; Schanze, K. S. Polymer-Based Chromophore−Catalyst Assemblies for Solar Energy Conversion. *Nano Convergence* **2017**, *4*, 37.
(30) Li, S.; Kim, S.; Davis, A. H.; Zhuang, J.; Shuler, E. W.; Willinger, D.; Lee, J.-J.; Zheng, W.; Sherman, B. D.; Yoo, C. G.; Leem, G. Photocatalytic Chemoselective C−C Bond Cleavage at Room Temperature in Dye-Sensitized Photoelectrochemical Cells. *ACS Catal.* **2021**, *11*, 3771−3781.
(31) Leem, G.; Keinan, S.; Jiang, J.; Chen, Z.; Pho, T.; Morseth, Z. A.; Hu, Z.; Puodziukynaite, E.; Fang, Z.; Papanikolas, J. M.; Reynolds, J. R.; Schanze, K. S. $Ru(bpy)_3^{2+}$ Derivatized Polystyrenes Constructed by Nitroxide-Mediated Radical Polymerization. Relationship Between Polymer Chain Length, Structure and Photophysical Properties. *Polym. Chem.* **2015**, *6*, 8184−8193.
(32) Shen, X.; Yao, M.; Sun, K.; Zhao, T.; He, Y.; Chi, C.-Y.; Zhou, C.; Dapkus, P. D.; Lewis, N. S.; Hu, S. Defect-Tolerant $TiO_2$-Coated and Discretized Photoanodes for > 600 h of Stable Photoelectrochemical Water Oxidation. *ACS Energy Lett.* **2021**, *6*, 193−200.
(33) Nayak, J.; Prabakar, K.; Park, J. W.; Kim, H. Effect of Synthesis Temperature on Structure, Optical and Photovoltaic Properties of $TiO_2$ Nanorod Thin Films. *Electrochim. Acta* **2012**, *65*, 44−49.
(34) Venkatraman, V.; Yemene, A. E.; de Mello, J. Prediction of Absorption Spectrum Shifts in Dyes Adsorbed on Titania. *Sci. Rep.* **2019**, *9*, 16983.
(35) Zhang, L.; Cole, J. M. Dye Aggregation in Dye-Sensitized solar cells. *J. Mater. Chem. A* **2017**, *5*, 19541−19559.
(36) Leem, G.; Morseth, Z. A.; Wee, K.-R.; Jiang, J.; Brennaman, M. K.; Papanikolas, J. M.; Schanze, K. S. Polymer-Based Ruthenium(II)

Polypyridyl Chromophores on $TiO_2$ for Solar Energy Conversion. *Chem. Asian. J.* **2016**, *11*, 1257−1267.
(37) Moia, D.; Cappel, U. B.; Leijtens, T.; Li, X.; Telford, A. M.; Snaith, H. J.; O'Regan, B. C.; Nelson, J.; Barnes, P. R. F. The Role of Hole Transport between Dyes in Solid-State Dye-Sensitized Solar Cells. *J. Phys. Chem. C* **2015**, *119*, 18975−18985.
(38) Choy, K. K. H.; Porter, J. F.; McKay, G. Langmuir Isotherm Models Applied to the Multicomponent Sorption of Acid Dyes from Effluent onto Activated Carbon. *Chem. Eng. Data* **2000**, *45*, 575−584.
(39) Langmuir, I. The Adsorption of Gases on Plane Surfaces of Glass, Mica and Platinum. *J. Am. Chem. Soc.* **1918**, *40*, 1361−1403.
(40) Yang, C.; Maldonado, S.; Stephenson, C. R. J. Electrocatalytic Lignin Oxidation. *ACS Catal.* **2021**, *11*, 10104−10114.
(41) Michaux, K. E.; Gambardella, A. A.; Alibabaei, L.; Ashford, D. L.; Sherman, B. D.; Binstead, R. A.; Meyer, T. J.; Murray, R. W. Visible Photoelectrochemical Water Splitting Based on a Ru(II) Polypyridyl Chromophore and Iridium Oxide Nanoparticle Catalyst. *J. Phys. Chem. C* **2015**, *119*, 17023−17027.
(42) Youngblood, W. J.; Lee, S.-H. A.; Kobayashi, Y.; Hernandez-Pagan, E. A.; Hoertz, P. G.; Moore, T. A.; Moore, A. L.; Gust, D.; Mallouk, T. E. Photoassisted Overall Water Splitting in a Visible Light-Absorbing Dye-Sensitized Photoelectrochemical Cell. *J. Am. Chem. Soc.* **2009**, *131*, 926−927.
(43) Bredar, A. R. C.; Chown, A. L.; Burton, A. R.; Farnum, B. H. Electrochemical Impedance Spectroscopy of Metal Oxide Electrodes for Energy Applications. *ACS Appl. Energy Mater.* **2020**, *3*, 66−98.
(44) Meng, K.; Thampi, K. R. Efficient Quasisolid Dye- and Quantum-Dot-Sensitized Solar Cells Using Thiolate/Disulfide Redox Couple and CoS Counter Electrode. *ACS Appl. Mater. Interfaces* **2014**, *6*, 20768−20775.
(45) Bai, Y.; Xing, Z.; Yu, H.; Li, Z.; Amal, R.; Wang, L. Porous Titania Nanosheet/Nanoparticle Hybrids as Photoanodes for Dye-Sensitized Solar Cells. *ACS Appl. Mater. Interfaces* **2013**, *5*, 12058−12065.
(46) Tasic, N.; Marinkovic-Stanojevic, Z.; Brankovic, Z.; Zunic, M.; Lacnjevac, U.; Gilic, M.; Novakovic, T.; Brankovic, G. Mesoporous $TiO_2$ Spheres as a Photoanodic Material in Dye-Sensitized Solar Cells. *PAC* **2018**, *12*, 374−382.
(47) Becker, M.; Bertrams, M.-S.; Constable, E. C.; Housecroft, C. E. How Reproducible Are Electrochemical Impedance Spectroscopic Data for Dye-Sensitized Solar Cells? *Materials* **2020**, *13*, 1547.
(48) Li, S.; Wijethunga, U. K.; Davis, A. H.; Kim, S.; Zheng, W.; Sherman, B. D.; Yoo, C. G.; Leem, G. Ru(II) Polypyridyl-Modified $TiO_2$ Nanoparticles for Photocatalytic C−C/C−O Bond Cleavage at Room Temperature. *ACS Appl. Nano Mater.* **2022**, *5*, 948−956.
(49) Wang, F.; Stahl, S. S. Electrochemical Oxidation of Organic Molecules at Lower Overpotential: Accessing Broader Functional Group Compatibility with Electron−Proton Transfer Mediators. *Acc. Chem. Res.* **2020**, *53*, 561−574.
(50) Rafiee, M.; Miles, K. C.; Stahl, S. S. Electrocatalytic Alcohol Oxidation with TEMPO and Bicyclic Nitroxyl Derivatives: Driving Force Trumps Steric Effects. *J. Am. Chem. Soc.* **2015**, *137*, 14751−14757.
(51) Ma, L.; Zhou, H.; Kong, X.; Li, Z.; Duan, H. An Electrocatalytic Strategy for C−C Bond Cleavage in Lignin Model Compounds and Lignin under Ambient Conditions. *ACS Sustain. Chem. Eng.* **2021**, *9*, 1932−1940.
(52) Beer, P. D.; Szemes, F.; Balzani, V.; Salà, C. M.; Drew, M. G. B.; Dent, S. W.; Maestri, M. Anion Selective Recognition and Sensing by Novel Macrocyclic Transition Metal Receptor Systems. $^1$H NMR, Electrochemical, and Photophysical Investigations. *J. Am. Chem. Soc.* **1997**, *119*, 11864−11875.
(53) Sun, B.; Chen, Y.; Tao, L.; Zhao, H.; Zhou, G.; Xia, Y.; Wang, H.; Zhao, Y. Nanorod Array of $SnO_2$ Quantum Dot Interspersed Multiphase $TiO_2$ Heterojunctions with Highly Photocatalytic Water Splitting and Self-Rechargeable Battery-Like Applications. *ACS Appl. Mater. Interfaces* **2019**, *11*, 2071−2081.
(54) Chen, Y.-L.; Chen, Y.-H.; Chen, J.-W.; Cao, F.; Li, L.; Luo, Z.-M.; Leu, I.-C.; Pu, Y.-C. New Insights into the Electron-Collection Efficiency Improvement of CdS-Sensitized $TiO_2$ Nanorod Photoelectrodes by Interfacial Seed-Layer Mediation. *ACS Appl. Mater. & Interfaces* **2019**, *11*, 8126−8137.
(55) Pan, Z.; Leem, G.; Cekli, S.; Schanze, K. S. Conjugated Polyelectrolyte-Sensitized $TiO_2$ Solar Cells: Effects of Chain Length and Aggregation on Efficiency. *ACS Appl. Mater. Interfaces* **2015**, *7*, 16601−16608.
(56) Fang, Z.; Eshbaugh, A. A.; Schanze, K. S. Low-Bandgap Donor−Acceptor Conjugated Polymer Sensitizers for Dye-Sensitized Solar Cells. *J. Am. Chem. Soc.* **2011**, *133*, 3063−3069.




https://doi.org/10.1021/acsami.1c20795
*ACS Appl. Mater. Interfaces* 2022, 14, 22799−22809